First measurements of oblique ECE with a real-time moveable line-of-sight on TCV

T.P. Goodman, V.S. Udintsev, I. Klimanov, A. Mueck, O. Sauter, C. Schlatter

Ecole Polytechnique Fédérale de Lausanne (EPFL)
Centre de Recherches en Physique des Plasmas
Association Euratom-Confédération Suisse
CH-1015 Lausanne, Switzerland

42 pages minus 15 for figure captions, tables and figures
1 table
11 figures (figures 3 and 6 should be in color)

Correspondance:

Timothy Paul Goodman
EPFL/FSB/CRPP
PPB224
Station 13
1015 Lausanne, Switzerland
+41 21 693 3490 (OFFICE)
+41 21 693 3487 (SECRETARY)
+41 21 693 5176 (FAX)

Email of corresponding author: timothy.goodman@epfl.ch

First measurements of oblique ECE with a real-time moveable line-of-sight on TCV

T.P. Goodman, V.S. Udintsev, I. Klimanov, A. Mueck, O. Sauter, C. Schlatter

Abstract. Electron cyclotron emission (ECE) radiometers viewing perpendicular to the magnetic field are common on nearly all tokamaks for measuring the electron temperature with good spatio-temporal resolution. Two such radiometers are installed on TCV; one looking from the low and the other from the high field side (LFS, HFS, respectively). The HFS radiometer is especially sensitive to non-Maxwellian emission in the presence of the strong electron cyclotron current drive (ECCD) provided by the 3MW second harmonic (X2) EC system, as the non-thermal radiation is not reabsorbed by the bulk when passing to the receiver. Simultaneous HFS and LFS measurements allow higher order modeling of the electron distribution function as more constraints are provided by the dual measurements; however, the asymmetric nature of the electron distribution function required for ECCD to occur, is not directly put in evidence by these lines-of-sight. Oblique ECE measurements of an asymmetric non-thermal electron distribution, on the other hand, are expected to also be asymmetric and can provide important information on the current carrying features of the non-thermal population. A dedicated receiving antenna has been installed allowing real-time swept oblique ECE on TCV in both the co- and counter- looking directions. Proof of principle experiments are described in which Doppler-shifted emission is measured.

INTRODUCTION

Low field side (LFS) and high field side (HFS) viewing lines from two heterodyne radiometers[1,2] have been used on the TCV tokamak (R_0=0.88m, a=0.25m, κ_{max}=2.8, B_0=1.5T) to diagnose the electron cyclotron emission (ECE) from plasmas heated with up to 3MW of electron cyclotron heating (ECH) and current drive (ECCD) (82.7GHz, 2nd harmonic X-mode (X2)). The dual observations, being primarily sensitive to bulk and suprathermal electrons, respectively, have been crucial to the understanding of experiments in which 100% absorption of 3rd harmonic X-mode radiation (118GHz, 0.5MW) was measured under specific X2-ECCD pre-heating conditions[3,4]. Furthermore, they have been used to demonstrate that a significant fraction of the magnetic energy released during the magnetic reconnection which occurs at the familiar sawtooth crash, can be transferred to fast-electrons[5].

In the interest of complimenting these viewing lines and enhancing the flexibility of the ECE system on TCV[6,7], a LFS launcher has been connected to the LFS radiometer via 1" circular waveguide and a microwave switch. One of the many possibilities opened up by this antenna is the ability to put into evidence the asymmetry in the electron distribution function generated during high power ECCD, by viewing the plasma with oblique ECE (i.e. with a viewing line which is not perpendicular to the magnetic field) [8]. This technique has been used on Tore Supra, PBX and the FTU tokamaks, and will soon be installed on JET[9]. This paper describes the experimental setup as implemented on TCV, and shows first measurements taken with the real-time-movable, oblique-viewing receiver, during ECCD. Preliminary calculations using the NOTECTCV radiation balance code are

presented. We investigate the dominant physics effects expected to be evidenced by the LFS oblique ECE, in a typical electron Internal Transport Barrier (eITB) discharge and discuss the limits under which the new line of sight can help pin down the electron distribution function (EDF).

LAUNCHER

A receiving antenna has been installed in TCV in sector 7 (of 16) which is identical to one of 6 existing X2 launchers[10]. The 4 mirrors of the launcher have been polished to allow laser alignment of the beam in the tokamak. Two of the mirrors are offset ellipsoids which provide focusing of a microwave beam launched from 63.5mm diameter, open-ended, corrugated waveguide (The propagation mode in the waveguide is principally the hybrid HE11 mode).

The antenna is seen in figure 1. The waveguide is attached at the left and the plasma would be to the right in this picture. The mirror orientation, relative to the table top is as in TCV, in the "rest" position (ϕ_L=0, θ_L = 55°). The subscript "L" refers to the launcher coordinates. From a purely operational point of view, these are the "control" parameters of the launcher. (The launcher coordinate system is spherical with the positive z-axis running horizontally inward along the axis of the TCV port; the x-axis points vertically downward. With the usual TCV toroidal field, ($\mathbf{B}_\phi$>0**),** and plasma current (I_p>0) configuration, ϕ_L> 0 generates electron cyclotron current driven in the same direction as the plasma current: co-ECCD.) The first (M1) and third (M3) mirrors along the beam path (from left to right) are sections of ellipses of revolution; the blackened back-side of the flat 2nd mirror (M2) (enhanced emissivity for cooling) is seen above the first mirror in figure 1. The movable 4th mirror (M4) is made of TZM, a machinable molybdenum alloy

with good electrical conductivity, low thermal expansion, high melting temperature and low sputtering yield. It is held above the 3rd mirror by a TZM rod passing through an extension of the vertical stainless-steel ring (A) which holds the 3rd mirror (far right). Mirror 4 pivots about this rod on silver-coated, stainless-steel, ball bearings when actuators, running though the long stainless steel tubes seen at each side (B), are pushed by the plate at the far left (C). The plate is advanced inward by the pistons of two linear vacuum feedthroughs (not shown), and outward by 4 restoring springs (3 are visible in the photo). The reference plane (D) for the springs (seen here butted against the table edge) is fixed in an extension of the TCV vacuum chamber by 4 bolts.

The 4-mirror structure, including the actuator rods, is rotated ($-180° < \phi_L < +180°$) about the axis of the input waveguide by gears turned by the rotation rod (E) seen at the top left (extending furthest to the left from the reference plane of the springs): A large gear, to which the stainless steel guide tubes are attached, is hidden behind the reference plane and two smaller gears are captured in the thick metal housing of the reference plane, at the right-hand end of the rotation rod. Ceramic elements made of ZiO_2 (ball bearings, washers and bushings) are used at appropriate places to avoid current loops. This material is resistant to thermal and mechanical shock and has high electrical resistivity. We will refer to this 4-mirror moveable structure as “the antenna”.

The antenna is mounted in the vacuum chamber (see Fig. 2) with the longitudinal axis (coincident with a waveguide axis) running inward, along a major radius of the torus at the midplane ($z=0$) of the machine; therefore, it is refered to as an equatorial antenna (2 other *launchers* are located in equatorial ports and 4 others in upper lateral ports 0.46m higher on the outer wall of the torus). Access to

the plasma is through a 0.148m diameter hole in the outer torus wall (to which the TCV ports were welded during construction). The 4th mirror (flat) of the antenna occupies part of this hole but, the innermost edge remains 2cm radially-outward of the carbon tiles in the main chamber (i.e. in the shadow of the tiles). For the beam to reach the plasma center, i.e. within the region where the safety factor q is less than 1, in typical plasmas, an angle of (θ_L) ~55° (relative to the major radial direction) is required. The 3rd mirror (focussing, made of oxygen-free high-conductivity (OFHC) copper) is blackened on the back side and also partially fills the hole; thus, the free space for passage of the beam is approximately 70mm. The beam crosses the hole at an angle of 55° and is clipped by these two mirrors at twice the electric field spot size (i.e. at a power level of -34.7dB). This places a constraint on the maximum allowable spot size at the output of the antenna.

As mentioned previously, the receiver antenna is identical to the high power launching antennas used to heat the plasma and to drive current. The HE_{11} mode of the 63.5mm diameter evacuated waveguide couples efficiently to a paraxial beam with Gaussian cross-section. The beam reflects from the 4 mirrors and exits the launcher at an angle to the launcher axis, determined by the angle of the 4th mirror (as seen in Fig. 2, the normals of all 4 mirrors are in one plane and the 4th mirror normal moves in that plane). The 4th mirror position can be adjusted rapidly to provide a **sweep** of the beam angle, relative to the major radius, between 7° and 55° within 500ms. At typical angles, this results in a deposition displacement of ~ 1mm/ms or, one full-width, half-maximum beam width in ~30ms when the EC resonance passes through the plasma center.

The design for the launching antennas was constrained by the need to install them in both equatorial and upper lateral ports due to port availability and

accessibility to the electron cyclotron (EC) resonance in the large variety of plasma shapes which are investigated in TCV. Some of the upper lateral ports are partially obscured by the mechanical re-enforcements of the torus magnet structure, which take the stresses induced during plasma disruptions. For ease of design and fabrication, and to produce interchangeable parts, the 7 launcher optics are identical. This leads to a large distance between mirrors in the launchers along the torus major radius and results in an overall structure which cannot be supported by the back-plate, i.e. closure-plate, of the vacuum chamber extension. (The installation of the launcher into the chamber also prevents this since a direct radial insertion is not possible). The launcher/antenna is, instead, attached to the main vacuum chamber extension and to ensure precise alignment, the antenna is also supported and constrained very near the pivot point of the 4^{th} mirror: forces generated during mirror actuation and disruptions are distributed from the stainless steel ring holding mirrors 3 and 4 onto ZiO_2 skates (bushings) fixed to the torus wall. A fourth, spring-loaded, metallic skate provides electrical grounding of the launcher mirrors and the associated, mobile, support structure to the torus.

The two degrees of freedom provided by the launchers give beam aiming which covers nearly the entire poloidal plane of TCV. When the beam is **swept** using mirror 4, the beam motion is not necessarily in either the poloidal, or the toroidal plane; the sweep is in a plane tilted to both the horizontal (toroidal) and vertical (poloidal) directions which depends on the **rotation** of the antenna about the major radius.

Finally, the output Gaussian beam waist of the launcher/receiver occurs very near the plasma edge (depending predominantly on the height of the plasma magnetic axis, z_{mag}, in the torus chamber relative to the height of the antenna axis –

$z_{antenna}$ = 0.0m or, 0.46m for the equatorial and upper lateral antennas, respectively.)

ECE RADIOMETER AND RECEIVER SETUP

Each gyrotron of the TCV ECH system transmits power to the plasma via a matching optics unit (MOU); window-less, 63mm-diameter, corrugated, Aluminum waveguide; the "straight-through" leg of a remote-controlled, high-power, microwave switch; an in-line, vacuum pumping section; an all-metal gate-valve; and a launcher.

Oblique measurements were taken through launcher 1 (X2L1), without venting the torus, prior to the installation of the 7th launcher (receiving) antenna (X2L7) (which required a torus vent). To do this, the section of the transmission line immediately before the launcher – between the high-power, vacuum, microwave switch and the tokamak – was removed. The switch has integrated gate-valves at each output port, so the rest of the transmission line was kept under vacuum and the gyrotron power was diverted to a calorimetric load, attached to the "diverted" leg. A short pumping section (100mm) and window (10mm thick Pyrex) were installed at the all-metal gate-valve entry to the launcher, the section was pumped and the gate-valve opened thus providing a view of the plasma via the launcher.

When X2L7 was installed, its gate-valve was replaced permanently by a 6mm thick, 100mm diameter, PYREX window so no additional pumping is required as the tokamak vacuum extends directly to the window. Several of the high power launchers can aim at the receiving antenna either directly, after reflection off the central column, or, by refraction, in the case of too-high density. Therefore, two microwave detectors are mounted on open-ended WR10 rectangular waveguide

near the edges of the X2L7 window. If the signal level exceeds a threshold, the gyrotrons are turned off. Additionally, a fiber-optic cable views the window and will shutdown the gyrotrons in case of an arc.

Polarization

EC radiation was received by open-ended, one-inch-diameter (over-moded), smooth, copper waveguide. For oblique ECE, the required polarization is elliptical; defined by the angles $\alpha_{optimum}$ (rotation of the major axis of the ellipse away from the direction of the magnetic field **B**) and $\beta_{optimum}$ (arctangent of the ratio of the minor to major axis of the polarization ellipse). These optimum polarization angles vary as a function of launcher angle, frequency and plasma equilibrium. The receiver polarization was constant and determined by one of the three waveguide configurations described below.

Initially, the geometry of the transmission line was such that a 22.5° rotation of the electric field away from the vertical resulted at the entrance to the antenna window (radiometer input projected to the end of the transmission line). This yielded α_{set} = -112.5° and, when added to the magnetic field line inclination resulting from the plasma current I_p = 250 kA (~13°), resulted in a polarization rotation of ~35° away from "quasi" X-mode (i.e. the wave polarization which would transform continuously, as the index of refraction parallel to the magnetic field $N_{//}$ is decreased, to X-mode at $N_{//}$=0). More recently, the transmission line has been modified so that the electric field is vertical at the antenna window (α_{set} = 90°, pure X-mode for $N_{//}$=0 and I_p = 0 kA).

The second polarization angle can be set to β_{set} = [-45°,0°,45°]. For the cases ±45° a "conversion section" consisting of a down-taper, circular-to-linear

polarizer, circular-to-rectangular waveguide, rectangular waveguide, rectangular-to-circular waveguide, and up taper was used at the exit of the receiver; for the case of 0°, it was removed. This section selects one helicity of the wave and reflects the other. The polarizer is a commercial product (Millitech 45866H-1001, center-frequency 82.6GHz). Without this converter, the received power is transmitted entirely through circular waveguide to a down-taper and circular-to-rectangular transition and finally a 4-port, low-power, rectangular-waveguide switch at the radiometer. The conversion section is near the antenna window for easy access and can be changed between shots. Unlike the high power launchers (see below), the subsequent mirrors in the oversized circular transmission line do not need to be taken into account when calculating the polarization as the helicity has already been selected and converted to vertical linear polarization.

The 4-port switch selects between three viewing line (perpendicular LFS via a lens at z=0.0 m, a horn antenna at z=0.21 m, or the X2L7 LFS antenna at $z_{antenna}$ = 0.0m). For a constant source power, switching between lines introduces ±0.09 (±2%) uncertainty in the calibration of the radiometer.

Coupling

The TCV ECH Control System (ECHCS) automatically calculates the optimum polarization required to couple to either quasi-X or quasi-O mode, hereafter referred to simply as X- or O- mode, as a function of the launch angles and the plasma configuration for all 6 X2 launchers. (In the case of power *launch* this information is relayed to the two remote-controlled, polarizer grating mirrors, in the matching optics unit (MOU) of each gyrotron, to ensure full absorption; generally, by coupling to the X-mode but in some experiments to the O-mode for O-X-B conversion to the electron Bernstein wave in over dense plasmas[8]. As the

MOU is attached directly to the gyrotron, upstream of the transmission line, the mirror reflections of the transmission line must be taken into account when calculating the polarization which needs to be set to match the optimum polarization at the plasma. For the receiver, the optimum polarization information is simply used to calculate the coupling of each (elliptically polarized) mode to the rectangular waveguide at the radiometer; depending on which converter section is used during the shot. That is, the coupling between the plasma source polarization ($\alpha_{optimum}$, $\beta_{optimum}$) and radiometer (α_{set} , β_{set}) polarizations are calculated automatically for each shot. The variation of β_{set} away from ±45° is not taken into account for the subsequent calculations. We note simply that the mode selectivity is improved with the polarizer in the correct orientation and that the variation with frequency is independent of the sign of $N_{//}$.

Figure 3 shows (central curve) the calculated coupling from the X mode (optically thick) for 2 early shots 27998 (co viewing direction) and 28000 (counter viewing direction) in which the circular polarizer was not installed but , in which $N_{//}$ was swept during each shot. The sign of $N_{//}$ was reversed between the two shots by rotating the receiver (e.g. $\phi_L = +90° \rightarrow \phi_L = -90°$).

The mode selection is poor – nearly equal O and X mode coupling to the radiometer. Poor mode selection results in a loss of localization in the radiation temperature measurement. Nevertheless, the variation of the coupling *from one shot to the other* is less than 0.5% over all angles and frequencies even though a more significant change in coupling is seen with time (i.e. angle) for each individual shot (Fig 3). As the calculations take into account the measured launcher and plasma configurations of each shot, the 0.5% variation indicates good shot to shot reproducibility of the overall launcher/plasma geometry. Relative

measurements can be made between different shots; introducing only negligible differences in the coupling to the radiometer due to the geometry. The same is true if circular polarization is used, provided the helicity is flipped for measurements having opposite viewing directions (e.g. β is changed from +45 to -45 when the view is rotated). Use of the circular polarizer will increase the X-mode signal by a factor of ~2 and provide better mode selectivity (X/O ≥ 4 at all angles – upper curves divided by the lower curves in figure 3) but at the same time results in additional front-end insertion loss due to the additional fundamental waveguide sections used.

Radiometer Calibration

The radiometer is not absolutely calibrated at present but a millimeter wave noise source will be installed in the future to allow this. To obtain a radiation temperature measurement, a cross calibration of the radiometer channels to the Thomson Scattering (TS) profiles is made for both the HFS and LFS radiometers, assuming Maxwellian electron distribution functions. The TS system has 35 optical fibers collecting light through three lenses on the outboard side of the machine. For the moderate elongation plasmas (k ~ 1.7) used in these experiments, typically 25 vertical TS points are inside the plasma. The measurements are taken every 50ms, but are not synchronized with the sawteeth. In stationary plasma conditions this leads to ±10% variation in the central temperature measurements and variations in the profiles shape from one TS measurement time to the next.

The ECE is altered by the generation of fast electrons at the sawtooth crash[3,6], especially for edge channels or if the optical depth is less than about three. If TS measurements fall within a certain time window after the crash, the ECE and TS profiles are not expected to be comparable; that is, some TS time slices are not

suitable for cross-calibration of the ECE channels. The time window to be excluded has been shown to be of the order of a few tens of microseconds following the crash in both EC-heated and Ohmic plasmas[3]. (During high power ECCD, fast electrons are always present and care must be taken to avoid downshifted emission from higher harmonics which may reach the radiometer; either due to low optical depth of the bulk (HFS view) or no absorption by the bulk (LFS view)).

Ideally, the calibration is done during pure EC heating; in this case, fast electrons are not present but, the temperature and thus the optical depth is higher than in Ohmically-heated plasmas. When this is not possible, cross-calibration is performed during the Ohmic phase of a TCV discharge, prior to the application of EC power. Then, the plasma edge region is optically grey or optically thin and the ECE measurements lack spatial resolution for these regions/frequencies.

The effect on the ECE intensity of radiation originating from an extended region of the plasma, arriving at the radiometer either directly or after reflection and polarization scattering from the walls, can be taken into account once the wall reflection coefficient is known.

With the antenna rotated (e.g. $\phi = \pm 90°$ - see figure 2) to allow a sweep of $N_{//}$ in the plasma midplane during one shot, it is not possible to view at $N_{//} = 0$; the minimum angle is $\sim \pm 10°$ or $N_{//} = \pm\ 0.17$. In some cases, TS data may not exist at the time when $N_{//}$ is smallest. Therefore for shots 27998 and 28000, three different calibrations are performed and compared with each other: *1)* standard cross-calibration done for each shot while the receiver is at small angle, prior to a sweep, *2)* the calibration of one shot is used for both shots, and *3)* the LFS channels are

cross-calibrated to the HFS channels during pure ECH, ignoring slight mismatches in the mapping of frequency to major radius for the 2 lines of sight[6].

All cross-calibration against TS supposes that both diagnostics measure the local bulk (Maxwellian) energy distribution and ignores potential differences between them[11]. Since our goal here is a qualitative, shot-to-shot comparison of shots with different viewing directions, in otherwise identical plasmas, this latter point is of small importance.

Calibration at small angle

First we define "small" as far as the calibration angle is concerned.

Note that even for the $N_{//} = 0$ case of a radiometer setup, there is typically a spread in $N_{//}$ due to the optics. This can be characterized by a ½ beam-angle defined for a paraxial Gaussian beam as *arctan(w(z)/R(z))*, where *w(z)* is the beam spot radius (e^{-2} power radius) and *R(z)* is the phase front radius of curvature, each measured at the distance $z = z_{res.}$; that is, the distance from the minimum beam waist to the resonance when viewing perpendicular to the vacuum **B** field. (Alternately, the -3dB ½ angle can be used. Note that the FWHM *diameter* is only 18% larger than the e^{-2} power *radius* for a Gaussian beam.) The divergence angle changes with frequency, magnetic field strength and viewing line. For the standard TCV field of 1.43T it ranges from ±3.6° for the oblique launcher (±1.4° if an 63.5mm diameter HE_{11} waveguide were to be used, as in the launch of power) to ±10.3° and ±12.4° for the LFS and HFS z=0.21m lines (mirror optics), respectively. Figure 4 shows an example of the measured beam spot (e^{-2} power *radius*) from the oblique receiver, as a function of the distance from the launcher, at 2 different frequencies. The solid curves show the evolution of the spot as fit to a paraxial beam. While the lower frequency beam is more divergent and larger

than the corresponding higher frequency beam at each distance, the radiation collected by the optics at 69.2GHz is pre-dominantly from a distance more than ~170mm closer to the LFS receiver (smaller path length in the figure) than for 82.7GHz. Therefore, the relevant beam size is estimated to be actually smaller at 62.9GHz. (If 63.5mm diameter HE_{11} waveguide were used, the beam size would be reduced by a factor of 2 from 52±10mm to 26±3mm over all frequencies).

For the LFS z=0 line (lens) the angle is ±2.1°. Refraction between the plasma edge and the resonance is not taken into account for these values but it is generally only significant for the oblique view at large angle or at densities near cut-off.

We note that the z = 0.21m viewing lines accept a significant spread in $N_{//}$. Nevertheless, after calibration during the Ohmic phase of a discharge, the temperature profiles measured during subsequent ECH with these lines do not deviate significantly from those measured by Thomson scattering. This indicates that the Doppler broadening of the emission line is not visible by the radiometer. As the angular spread from the LFS oblique receiver viewing at the minimum attainable angle of 10° would have a maximum -3dB angle of 13.6° (compared to 12.4° for the HFS view) it, too, is likely to be acceptably unbiased by Doppler-shifted emission. Small angle calibration can be carried out at 10° from radial without significant perturbation from any fast electrons which may be present.

Finally, for some plasma/launcher configurations, it is possible for the view to be tangent to the flux surface on which the magnetic field lines lie. In this case, the field line angle is directly translated into an equivalent $N_{//}$ and can amount to several degrees. While is has been shown that the small Doppler shift resulting from this angle can play a significant role in the physics of sawtooth stabilization during poloidal plane heating[12], by the arguments given above the effect of this

small angle should also be negligible for ECE measurements during ECH. Here we note that in all cases, the Doppler broadening is in addition to the relativistic broadening due to the temperature.

One Shot Calibration

The HFS view is the same for all shots and the plasma location does not change relative to the antenna. In steady state, the entire pulse (up to 100 TS measurements) may be used for cross-calibration to TS. Each time slice is calibrated independently. The typical standard deviation of the point TS measurements over 100 profiles is +/- 5% in steady state. Part of this fluctuation is due to the sawtooth instability, is therefore "real", and should be seen also by the ECE measurements; the rest is due to photon statistics.

The TS data is collected along a vertical line through the plasma whereas the ECE comes from a horizontal view. In order to cross-calibrate, the measurement regions of both diagnostics are mapped onto the normalized minor radius of the plasma equilibrium assuming poloidal symmetry. During the sawtooth crash and mode activity on the q=1 (or other) surface this symmetry is broken, as indicated by soft X-ray tomography[13]. The local temperature of each diagnostic will deviate from the poloidally-averaged value in different ways. These fluctuations set a lower limit on the accuracy of the cross-calibration.

For the oblique receiver, the viewing line is swept during the shot; therefore, far fewer TS measurements (e.g. for shot 27998, 28000 only 2) are available in steady conditions. Figure 5 shows this equivalence for shots 27998 and 28000 prior to application of EC power. Using the same ECE calibration factors for both shots yields acceptable matches of the ECE and soft x-ray temperatures as well as

profiles which are within the expected standard deviations of the TS measurements at least at small enough angles.

LFS to HFS Cross-Calibration

The HFS radiometer channels partially overlap those of the LFS. In contrast to the TS measurement, comparing the 2 sets of *radiometer* signals is not plagued by flux averaging when dealing with non-poloidally symmetric events (e.g. tearing modes). On the other hand, if these events engender strong perturbations of the EDF (e.g. sawtooth crashes), the differing viewing directions result in signals weighted more strongly to the high or low energy electrons. Nevertheless, owing to the higher acquisition rate of the radiometers and the fact that the HFS line-of-sight viewing angle is fixed in time, there will likely be several TS measures which can be compared with the HFS radiometer for calibration. As the HFS measurement will also be available at the times for which the LFS angle is small – even if TS is lacking at these same times – the LFS can be cross-calibrated to the HFS.

EXPERIMENTS

Three shots were carried out initially; two with ECH heating and co- or counter-viewing; and one with ECCD in the co-direction (i.e. ECCD in the same direction as the plasma current). During each of the shots, the input power configuration was constant in time (power and injection angles); while the LFS viewing angle was swept from 10° to 35° over 1s; once looking in the co-direction and once in the counter-direction. The first 2 shots had β=0° and were used to establish the reproducibility of the plasma as well as the difference in the ECE spectra measured when *viewing* a symmetric electron distribution function in *opposite directions*.

(Although there is an asymmetry due to the bulk drift velocity associated with the plasma current, this is negligibly small when no suprathermal electrons are present; or, at least, can be considered equivalent to a systematic "error" on the symmetry of the ECE spectra.)

The ratio of the low-pass-filtered HFS signals (fixed viewing line) from one shot to the next during ECH is 1±10% over all radii (frequencies) and times. The ratio of the LFS signals also varies by about ±10% except at the largest toroidal angles where refraction becomes important and even small differences in density between the two shots are accentuated. This shot-to-shot variation is similar to the variation of kinetic quantities measured by other diagnostics (e.g. Thomson Scattering and the diamagnetic loop). In future experiments, shot-to-shot ratios of LFS signals greater that ±10% when viewing in opposite directions (i.e. with a sign change in $N_{//}$) can be considered to be statistically significant – i.e. not due to irreproducibility between discharges.

A second pair of similar shots was executed using good X-mode selectivity and *swept co-viewing* (+10° to 30°; β=45°) for both discharges. No change in the transmission line system to the LFS radiometer was required as both were *co-viewing* and use the same β. Low power (250kW), small angle, ECCD was injected, once in the co(-10°) and once in the counter (+10°) directions. We note that the radiation temperature of each shot initially tracks the TS temperature, but decreases slightly with angle in each shot. The ratio of the LFS signals (cnt-eccd/co-eccd) was again calculated. It slowly decreases with increasing viewing angle, from 1.0 to 0.85, at all optically thick frequencies. This type of shot comparison is different than keeping the same electron distribution function (EDF) and simply viewing it in opposite directions for the same plasma equilibrium.

Here, we have kept the same view but attempted to change the EDF between shots. Care must be taken when comparing plasma having co-ECCD to those with counter-ECCD as the current drive alters the safety-factor profile and the local driven currents. For example, it is well known that the heating associated with counter-ECCD is enough to cause the loop voltage to *decrease* under I_p feedback as the change in conductivity and the very high current drive efficiency of the Ohmic transformer more than compensates for the counter driven current. Even slight difference are evidenced by changes in the MHD of the plasma but, they are not always evident in the reconstructed plasma equilibria. Mapping of frequency onto the equilibria can be different in each shot.

The measurement is now more localized and the decreasing *ratio* might be an indication of an asymmetry in the EDF but is not much different than the previous pair of higher power ECH shots in which the 2 plasma are expected to be equivalent to each other. We cannot rule out that the small difference in the ratio between these two ECCD shots is due to differences in the plasma equilibria rather than the EDF alone.

When higher power (500kW) co-ECCD at larger angle (25°) is injected centrally, we compare the maximum in the LFS emission relative to the discharge with 500kW ECH for the same viewing angle sweep: unfortunately, due to gyrotron arcing and lack of machine time, the matching discharge with the opposite -25° view is not available. The frequency of maximum emission intensity increases with angle (Fig. 6) in the co-ECCD case; whereas, it remains very nearly constant during the ECH discharge. These measurements provide a first clear indication of significant Doppler-shifted emission due to the non-thermal electrons[2].

NOTECTCV SIMULATIONS

The NOTECTCV code is also used to investigate the feasibility of LFS oblique ECE in TCV plasmas with high power ECCD. This code is an upgrade of the NOTEC code used for the ECE spectra simulation in RTP[14] and TEXTOR[15]. A previously studied discharge in which large n=0 oscillations where excited was chosen as an example. In TCV shot #32035, the plasma was placed at z=0, directly in front of the ECE launcher. Two EC beams (0.5MW each) provide co-ECCD off-axis at $\rho \approx 0.4$. Another EC beam (0.5MW) creates a hollow current profile with counter ECCD on the plasma magnetic axis $\rho = 0$. A high-temperature electron internal transport barrier (eITB) is established at very low loop voltage (plasma current feedback is still used). With this scenario, if the barrier is strong enough, a high frequency MHD mode can stimulate low frequency oscillation of an n=0 nature[7]. Similar oscillations have been reported experimentally on Tore Supra[16] and in simulations[17]. Common features on each machine are strong non-inductive current drive, very low loop voltage and the presence of an ITB.

Simultaneous HFS and LFS ECE (perpendicular) measurements of shot 32035 have been simulated to deduce the temperature, density and localization of one or two suprathermal electron populations in addition to the bulk. The equation of radiative transfer in the plasma is solved by NOTECTCV assuming a multi-bi-Maxwellian model for the EDF. The bulk temperature is set to the TS value and the TS density is used as the total electron density. One or several additional suprathermal populations are assumed to exist, each with associated perpendicular and parallel temperatures; $T^s_{\perp}$ and $T^s_{//}$, respectively; where s = 1,2,3, … depending on the number of suprathermal populations considered. The density of each population is given as a fraction of the total density and the spatial extent of each

population is specified by defining upper and lower limits in ρ where the population is present. For simplicity, the profile is simply scaled from the bulk profile and set to zero outside of the limits in ρ. In this way, a model EDF which is consistent with both ECE views has been found for shot 32035. It uses only one suprathermal population so the superscript *s* is dropped for the remainder of this paper.

At present, an automated fitting procedure which minimizes the errors (e.g. least squares fit) between the simulated and measured radiation temperatures has not yet been implemented. This will be done in the future. For our purposes here, we simply take the model EDF from reference 7 as a reasonable starting point for oblique ECE investigation and ask ourselves what might we expect to measure given this EDF. Clearly, if several different EDFs are equivalent for HFS, LFS perpendicular measurements but yield different results for oblique ECE, then the oblique ECE diagnostic will help to better constrain the choice of EDF.

NOTECTCV includes relativistic, multiple harmonics, polarization scrambling multiple wall reflections, 3D multi-ray tracing (cold plasma approximation), O- or X-mode branches, measured bulk temperature and density profiles, multiple bi-Maxwellian populations and, most importantly for this study, electron drift velocity (normalized to the speed of light $\beta_d \equiv v_{drift}/c$) for the suprathermal population(s). For the calculations presented here, the plasma equilibrium is taken as circular in the poloidal plane. NOTECTCV is being adapted to consider the actual TCV equilibria.

The EDF of shot 32035 is defined by the measured bulk and one suprathermal population with maximum density 5% that of the bulk, limited to the center of the plasma, $0 \leq \rho \leq 0.5$, roughly inside the barrier and off-axis ECCD deposition

location. Within the ρ limits, the non-thermal population has the same profile characteristics as the thermal (bulk) population. The bulk distribution is Maxwellian with peak central temperature T_b = 6keV, and density $n_b = 1.8 \bullet 10^{19} m^{-3}$, and the suprathermal distribution is bi-Maxwellian with $T_\perp$ = 57keV and $T_{//}$ = 15keV. The suprathermal temperature profiles are flat across the plasma (previous hard X-ray measurements justify this temperature profiling[18]). We note here that the choice of $T_{//}$ is arbitrary for the perpendicular views used in reference 7. (The bulk temperature profile as a function of frequency is shown by the squares in figure 9 for shot 32035.)

As the eITB plasmas in TCV tend to be run at low density, the optical depth of the bulk plasma near the plasma periphery can be small; therefore, we first compare results from NOTECTCV using 1, 2, 3, 5 and 7 wall reflections. Figure 7 shows that except at the highest frequencies ($f \geq 92$GHz), the simulated radiation temperature (receiving X-mode) is insensitive to wall reflections (only 1, 2, 5 are shown). At these high frequencies, 3 wall reflections are sufficient to take into account the expected enhancement of the radiometer signal due to the low optical depth at the edge.

Next, we compare LFS oblique ECE at ±20° off-perpendicular with $\beta_d = 0$. Figure 8 shows that, as expected, with a symmetric (in $v_{//}$) distribution function, the co and counter oblique views are equivalent to each other yet, differ substantially from the perpendicular view. The difference between the LFS ⊥ ECE and LFS oblique ECE already provides additional information to constrain the model EDF. In particular, the radiation temperature is seen to decrease at all frequencies and the maximum of the profile is upshifted by about 1.5GHz (90GHz to 91.5GHz). This can be understood by considering the fact that for the model EDF $T_{//} < T_\perp$ and the

resonance curve for oblique viewing on the LFS of the cold resonance is an shifted ellipse centered to one side of $v_{//}$=0 when plotted in normalized velocity space (e.g. see ref. 19 – u = γv/c, where γ is the relativistic mass factor, v is the electron velocity and c the speed of light). Therefore, oblique ECE will measure a radiation temperature which is a weighted average of the $T_{//}$ and $T_{\perp}$, in contrast to the purely perpendicular measurements. This is illustrated in figure 9 where the three cases $T_{//}<T_{\perp}$, $T_{//}=T_{\perp}$, and $T_{//}>T_{\perp}$ are compared. For each case, the EDF normalization product ($T_{\perp}\bullet T_{//}^{1/2}$) is kept constant. The 2 upper curves are those shown in the figure 8, this time along with the experimental points for the LFS lens viewing line (perpendicular). Given the scatter in the data and the EDF used to model this shot, an oblique view measurement would not strongly impact the choice of the best-fit EDF. On the other hand, if we compare the shapes of the lower 2 curves, the difference between the perpendicular view (+) and oblique view (stars) is striking; so, the availability of an oblique view should provide constraints on the $T_{\perp}/T_{//}$ ratio. Using the Maxwellian distribution function, the perpendicular and oblique view radiation temperatures are approximately the same (lozanges and circles, respectively), as expected for optically thick plasmas in which the decrease of the emissivity with angle predominantly shifts the location from which the radiation appears to originate, leading to a shift in the profile. It is clear from figure 9 that oblique ECE would help to better determine the ratio of $T_{\perp}$ to $T_{//}$ even for a symmetric (about $v_{//}$=0) EDF.

Finally, a drift, β_d = 0.2, is added to the original suprathermal distribution ($T_{\perp}$ =57keV, $T_{//}$ = 15keV) and it is seen (Fig. 10) that now a clear difference appears between the co- and counter-viewing radiation temperatures; the one being enhanced and the other decreased relative to the β_d = 0 case. The largest change

occurs at frequencies higher than ~80GHz for this particular shot. From our previous discussions, differences between shots of more than ±10% can be considered statistically significant. This would be true for frequencies above ~82GHz for the example in figure 10. In figure 11, the β_d is varied and the data is presented directly as a ratio of the co- to counter- viewing. The sensitivity limit of 10% is shown as a dotted line. From this figure we see that for drift velocities greater than about $\beta_d > 0.05$, oblique ECE can start to provide useful drift information at frequencies below ~70GHz and frequencies above ~90GHz. If all the plasma current were carried by the suprathermal population, it is estimated that for typical eITB plasma currents of 150kA the β_d is approximately 0.1 and co-/counter- viewing oblique ECE measurements should evidence the ECCD.

CONCLUSIONS

A LFS real-time movable ECE receiver has been successfully installed and used to measure Doppler-shifted suprathermal electron emission during ECCD by oblique viewing. Good shot-to-shot reproducibility has been confirmed allowing relative measurements between co- and counter- viewing despite the lack of absolute radiometer calibration. In the near future we plan to increase the measurement sensitivity by reducing the transmission line insertion loss and adding low-noise amplification. We will also complete a data set of co- and counter- viewing sweeps during strong ECCD at several difference ECCD injection angles and locations in discharges with, and without, eITBs. It is expected that these measurements should provide direct evidence of the EDF perturbation created by the ECCD. The NOTECTCV code provides a good tool for simulating and analyzing the ECE signals. It includes most of the important

physical and experimental effects such as multiple drifting suprathermal EDF's, multiple wall reflections and 3D multi-ray tracing for oblique ECE viewing.

ACKNOWLEDGMENTS

The authors gratefully acknowledge early work by Mark Henderson on the X2 launcher; and Rob Patterson, Kathryn Mason and Laurie Porte for low power measurements with the 1" waveguide. This work was partly supported by the Swiss National Science Foundation.

TABLE I. Antenna comparison – ECE viewing lines.

Radiometer	Viewing line	½ angle at e^{-2} power
HFS	z=0.21m	12.4°
HFS	z=0.00m	12.4°
LFS	z=0.21m	10.3°
LFS	z=0.00m (TPX lens)	2.1°
LFS	oblique moveable receiver	3.6°

FIGURE CAPTIONS

FIGURE 1. Two X2 launching antennas. Behind is a newer version with fewer components allowing easier construction. In the foreground the 4 mirrors (M1-M4) of the launcher/receiver can be seen in what would be their rest positions if mounted in TCV (ϕ_L=0, θ_L = 55°). Items indicated in the text: (A) M3,4 holder with M4 pivot axis, (B) M4-actuator guides, (C) M4 actuator plate, (D) reference plane, (E) 4-mirror rotation actuator rod.

FIGURE 2. Cut-away view of the launcher mounted in the vacuum chamber. For the receiver (7th launcher), the all-metal gate valve is replaced by a window and no indentation for the TCV structure is required. Historically, the angles θ and ϕ are referred to as "poloidal" and "toroidal" launcher angles (the subscript "L" is used in the text to indicate that these refer to the launcher coordinates). At a given theta, the beam path describes a cone as phi is swept through 360°. The inset shows a view from inside the torus of the last mirror and the actuator arms sticking through the opening in the outer vessel wall when rotated to -90°. The edge of the carbon tiles can be seen as a square around the opening.

FIGURE 3. a) Calculated fraction of the plasma radiated power coupled from the X-mode to the receiver as a function of measured launcher angles for two shots, with the minimum, maximum and mean radiometer channel-frequency as a parameter. Experimental plasma and launcher angle data are taken from shots 27998 and 28000. b) In the top 3 curves, the optimum circular-to-linear converter orientation has been selected: for shot 27998, β = +45° (for shot 28000 the optimum converter orientation is reversed (β = -45°) because the receiver views in the opposite toroidal direction). The lower curves show the resulting coupling for β = +45° (converter in wrong orientation) for shot 28000. The actual couplings for both shots corresponded to the a) curves in the figure during a mirror sweep.

FIGURE 4. Paraxial beam fit to the measured beam waist (o) as a function of distance after the X2L7 receiver for 69.2GHz and 82.7GHz. The distance to the LFS plasma edge

FIGURE 5. ECE profiles for shots 27998 and 28000 prior to ECH [0.5s to 0.6s] and during central ECH [0.75s to 0.9s] using the cross-calibration-to-TS factor determined for shot 27998 during the Ohmic phase. Time averaging is done to cover several sawtooth periods. The error bars are ±standard deviation of the signal during the averaging period and are somewhat smaller than for the TS due to the significantly smaller number of time samples during the intervals (only 3 to 4 TS profiles).

FIGURE 6. Radiation temperature from X2L7 radiometer during a real-time sweep of the co-view under constant current drive conditions (500kW co-ECCD). The viewing line is swept linearly from 10° at 0.7s to 32.8° at 1.1s. The maximum radiation temperature shifts from ~75GHz to ~87GHz during the sweep while the HFS radiometer sees no shift in the same shot.

FIGURE 7. Expected radiation temperature for X2L7 radiometer for the EDF of shot 32035 [ref. 7, $T_{\perp}$=57keV, $T_{//}$=15keV, 5% of bulk between 0 and ½ radius] but with a normalized drift velocity of $\beta d = 0.2$ measuring at 20° away from perpendicular. The calculations include multiple wall reflections. Below 92GHz the profiles are identical. At frequencies greater than 92GHz, the signal increases as more wall reflections are included. The plasma center is indicated by the arrow and the region for which the thermal-bulk optical-depth is greater than 3 is bounded by the vertical lines.

FIGURE 8. Calculated radiation temperature from X2L7 radiometer for the EDF of shot 32035 [ref. 7] with no normalized drift velocity i.e. $\beta d = 0.0$. The calculations include no wall reflections. The co- and counter- viewing profiles are equivalent. The oblique views result in lower radiation temperatures due to the bi-Maxwellian nature of the EDF: $T_{//}<T_{\perp}$.

FIGURE 9. Squares show the TS measured bulk temperature profile mapped to equal flux surfaces as the radiometer frequencies. Triangles indicate the measured radiation temperature using the LFS lens (perpendicular) viewing line [ref. 7]. The 6 curves with symbols show 3 pairs of calculated radiation temperatures as would be measured by the X2L7 radiometer viewing at 0° (x, lozanges, +) and 20° (*,circles, stars); each pair using a different bi-Maxwellian distribution with ($T_{\perp} \bullet T_{//}^{1/2}$)

constant and no drift. For the upper curves $T_{//}<T_{\perp}$ (15keV<57keV), as in figure 8; lower curves: $T_{//}>T_{\perp}$ (88.9keV>23.4keV i.e. the inverse ratio of the previous set) and middle curves: $T_{//}=T_{\perp}$ (=36.5keV). Only for the maxwellian distribution are the profiles of similar magnitude. The oblique viewing line provides general information about the parallel energy of the electrons, as expected; even for a symmetric (no-drift) distribution.

FIGURE 10. Calculated radiation temperature from X2L7 radiometer for the EDF of shot 32035 [ref. 7] but with a normalized drift velocity of $\beta d = 0.2$. The calculations include 5 wall reflections. A clear difference is evident between the two opposite off-perpendicular views (±20°). Oblique ECE evidences the current carrying portion of the EDF. The upper curve in this figure is the same as in figure 7. This figure should be compared to figure 8 which has no drift..

FIGURE 11. The ratio of co- to counter- viewing oblique ECE with normalized drift velocities of $\beta d = 0.05$, 0.1 0.2. Values greater than the dashed line can be considered statistically significant; $\beta d>0.05$ in the experiments of this example.

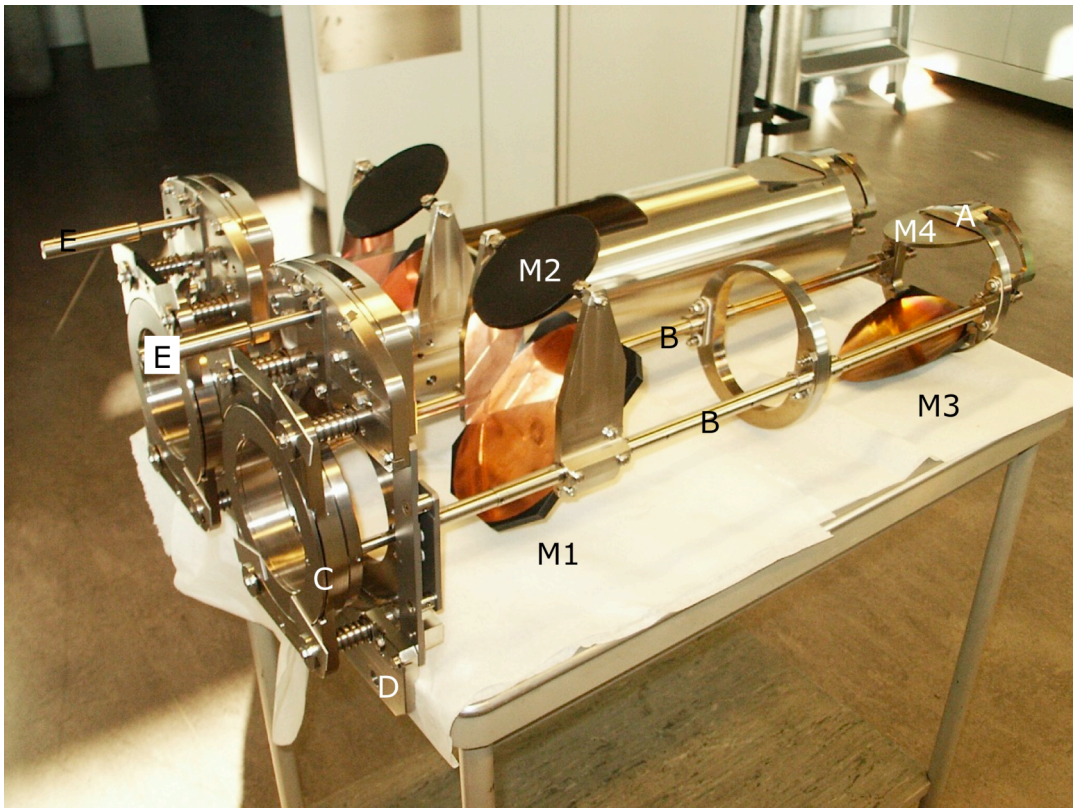

First measurements of oblique ECE with a real-time moveable line-of-sight on TCV,
TP Goodman, Figure 1

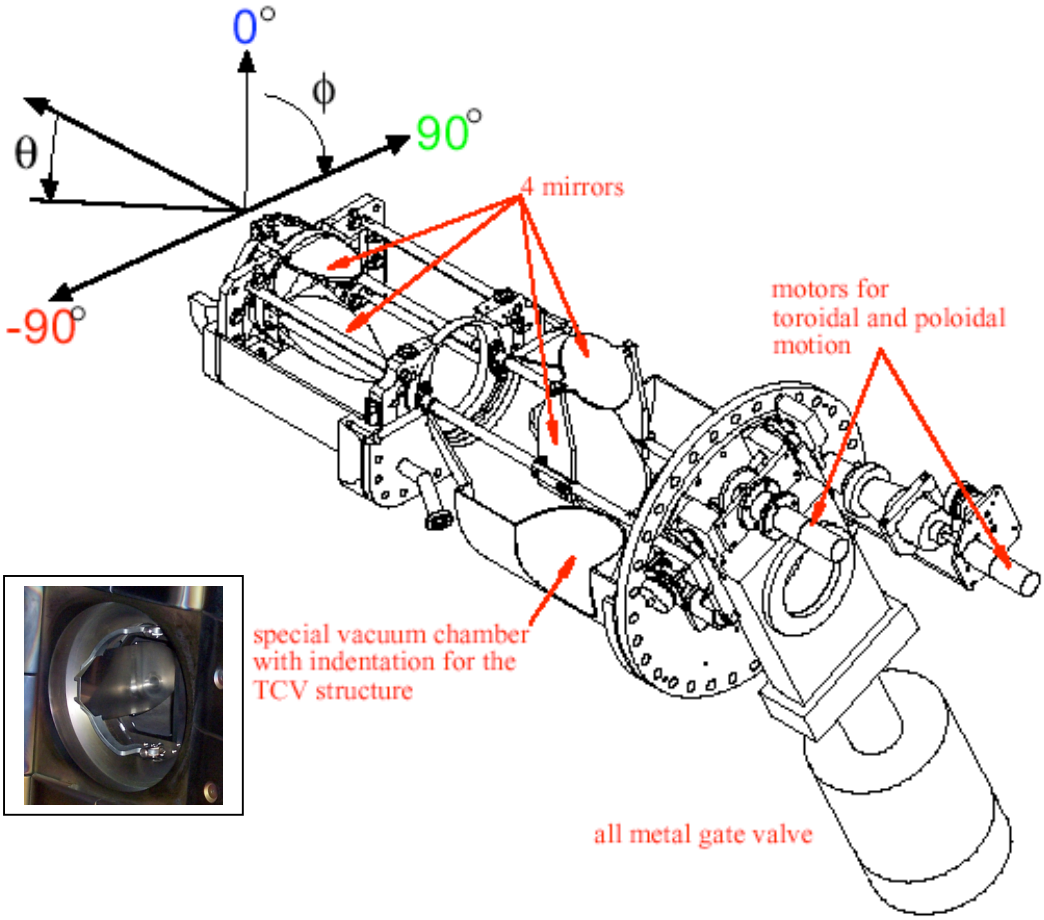

First measurements of oblique ECE with a real-time moveable line-of-sight on TCV,
TP Goodman, Figure 2

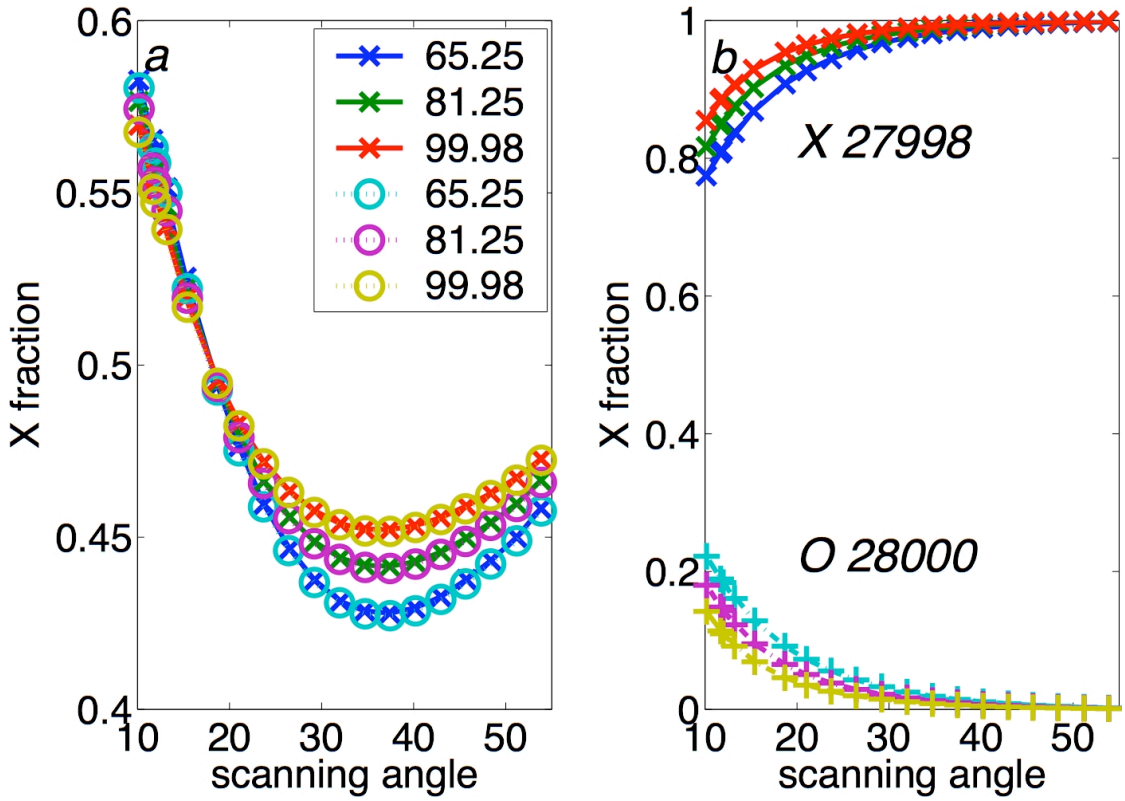

First measurements of oblique ECE with a real-time moveable line-of-sight on TCV, TP Goodman, Figure 3

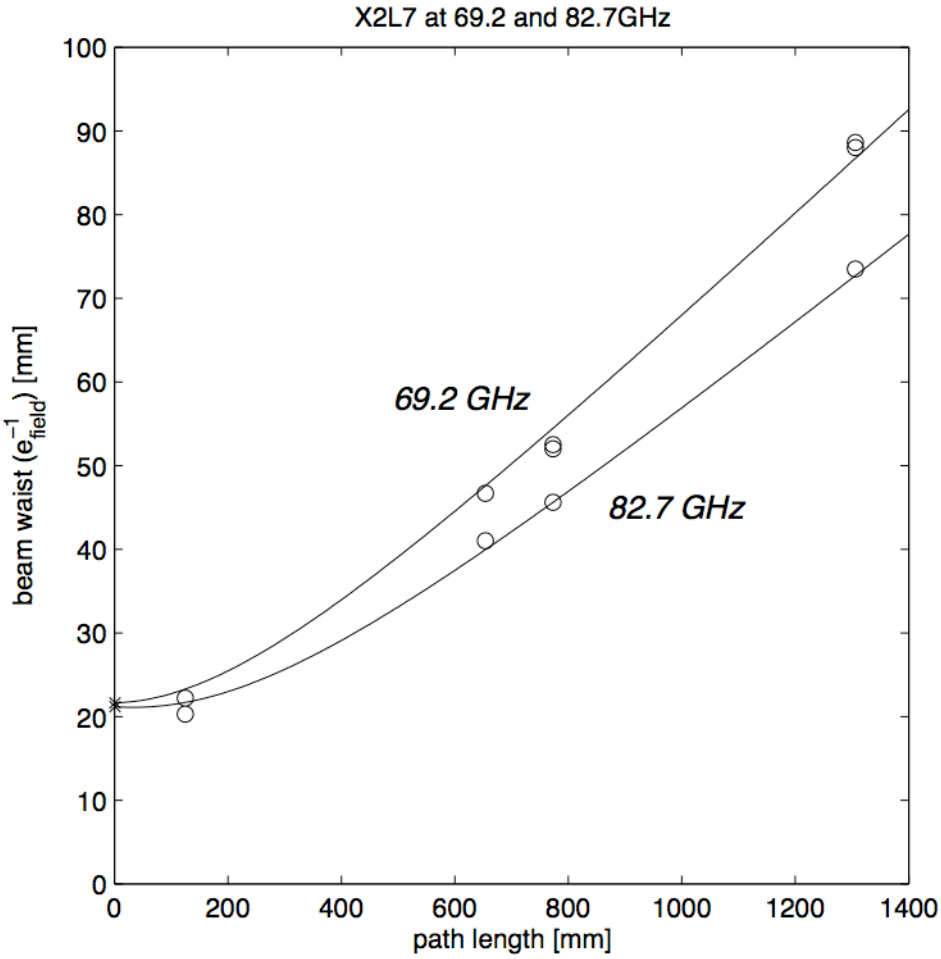

First measurements of oblique ECE with a real-time moveable line-of-sight on TCV, TP Goodman, Figure 4

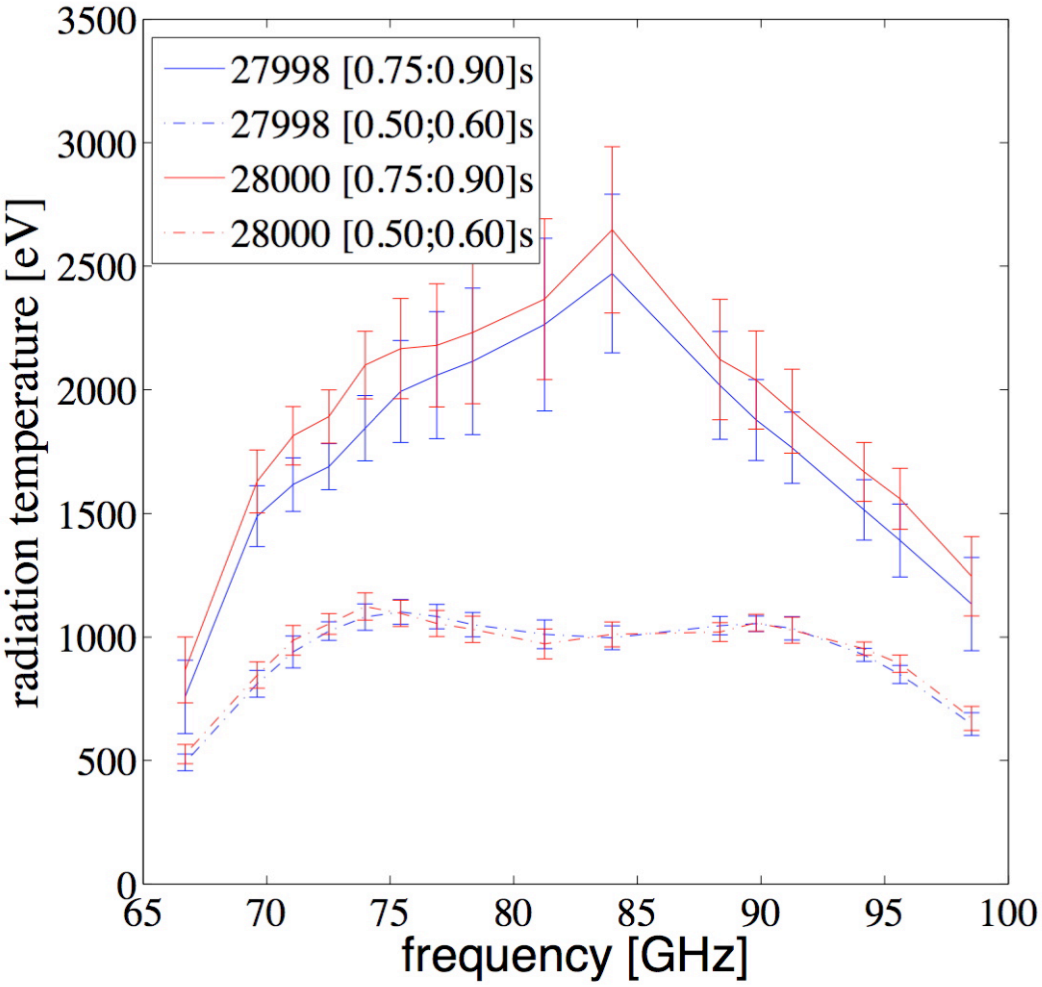

First measurements of oblique ECE with a real-time moveable line-of-sight on TCV, TP Goodman, Figure 5

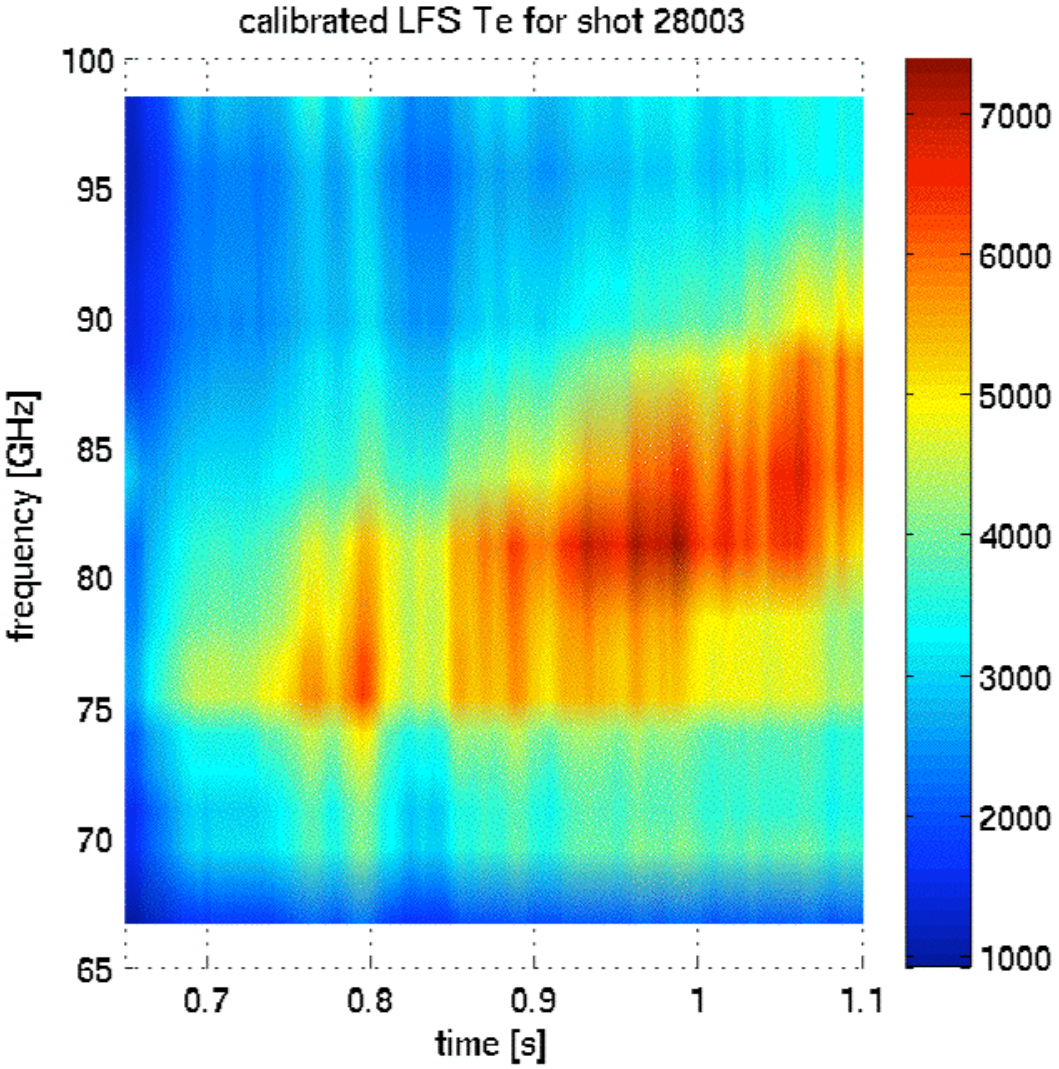

First measurements of oblique ECE with a real-time moveable line-of-sight on TCV,
TP Goodman, Figure 6

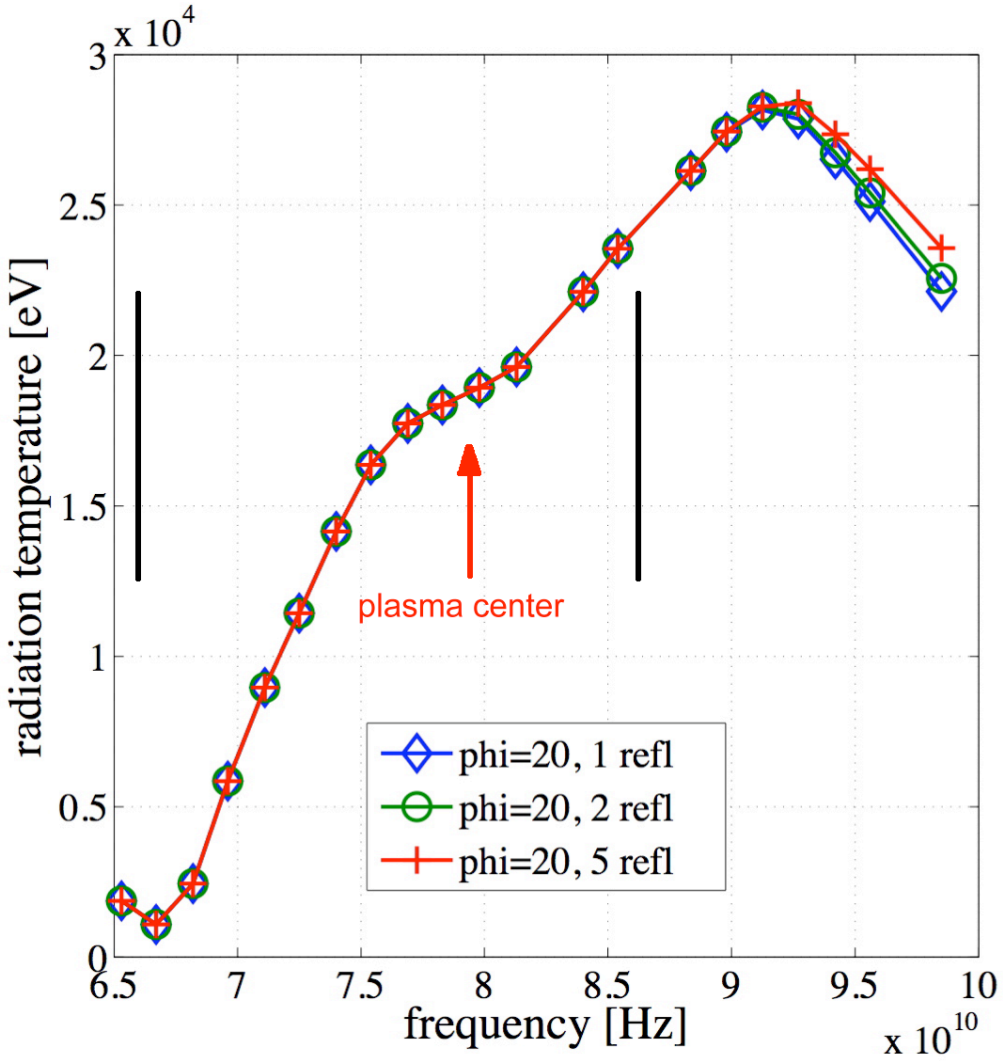

First measurements of oblique ECE with a real-time moveable line-of-sight on TCV, TP Goodman, figure 7

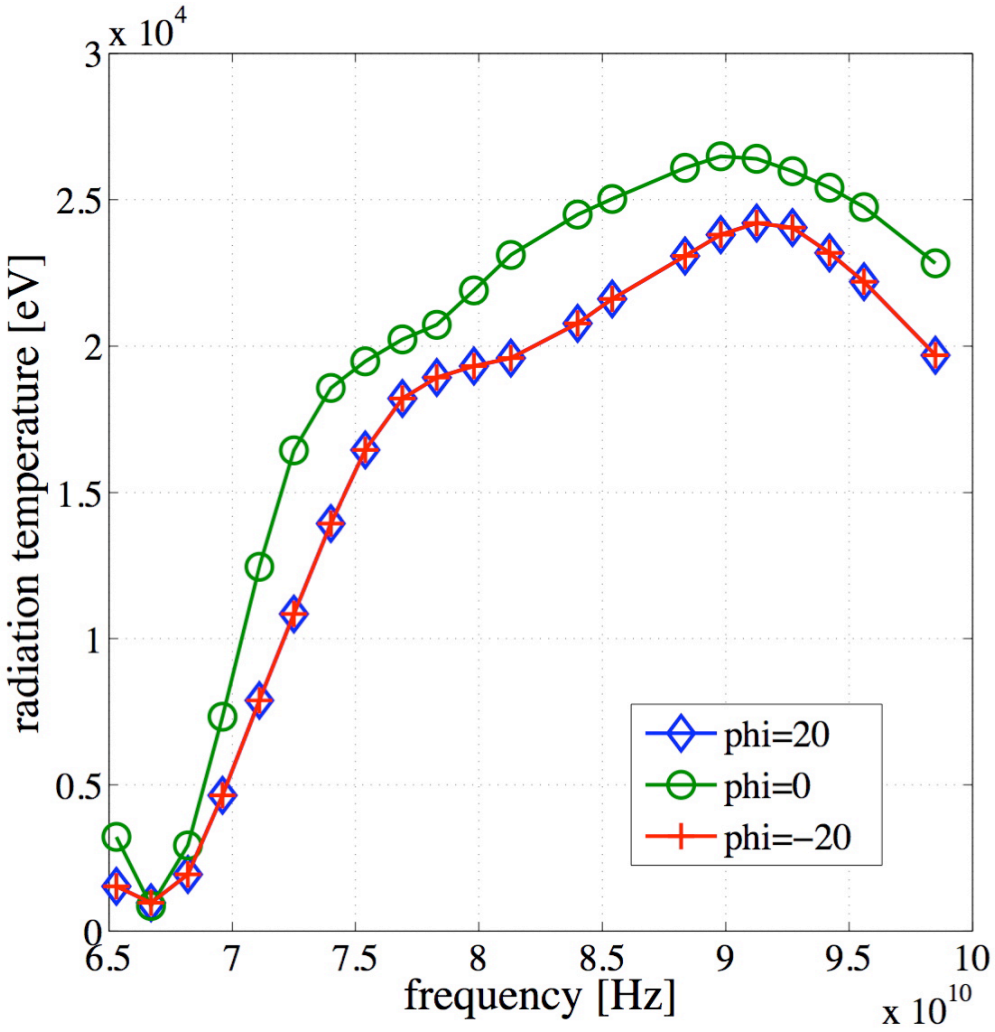

First measurements of oblique ECE with a real-time moveable line-of-sight on TCV, TP Goodman, figure 8

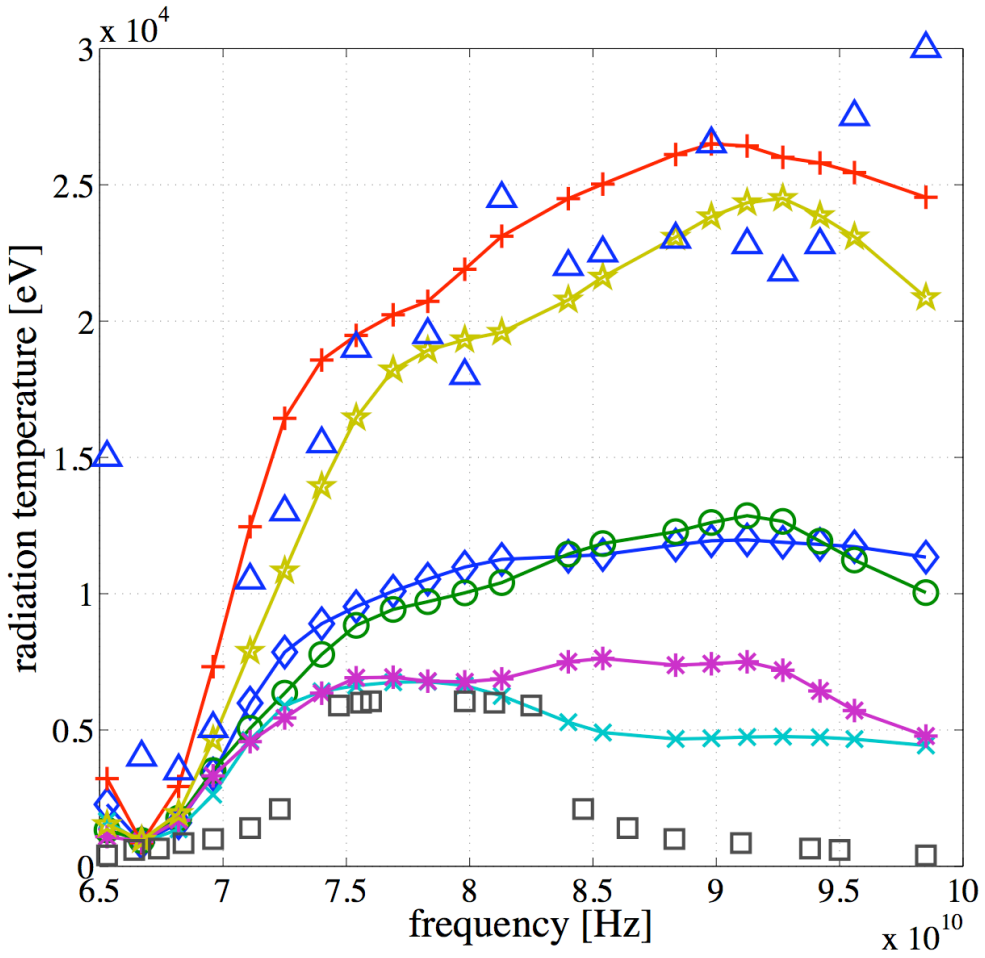

First measurements of oblique ECE with a real-time moveable line-of-sight on TCV, TP Goodman, Figure 9

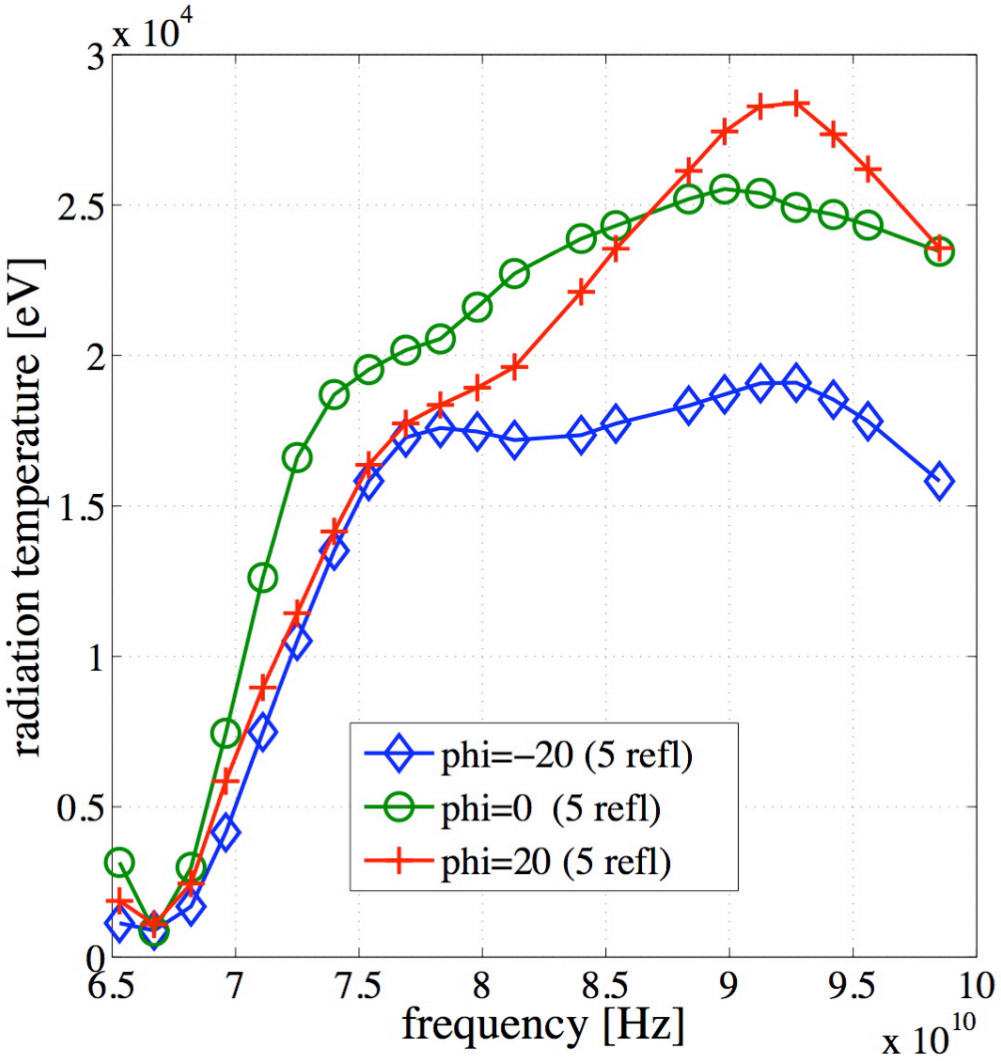

First measurements of oblique ECE with a real-time moveable line-of-sight on TCV, TP Goodman, figure 10

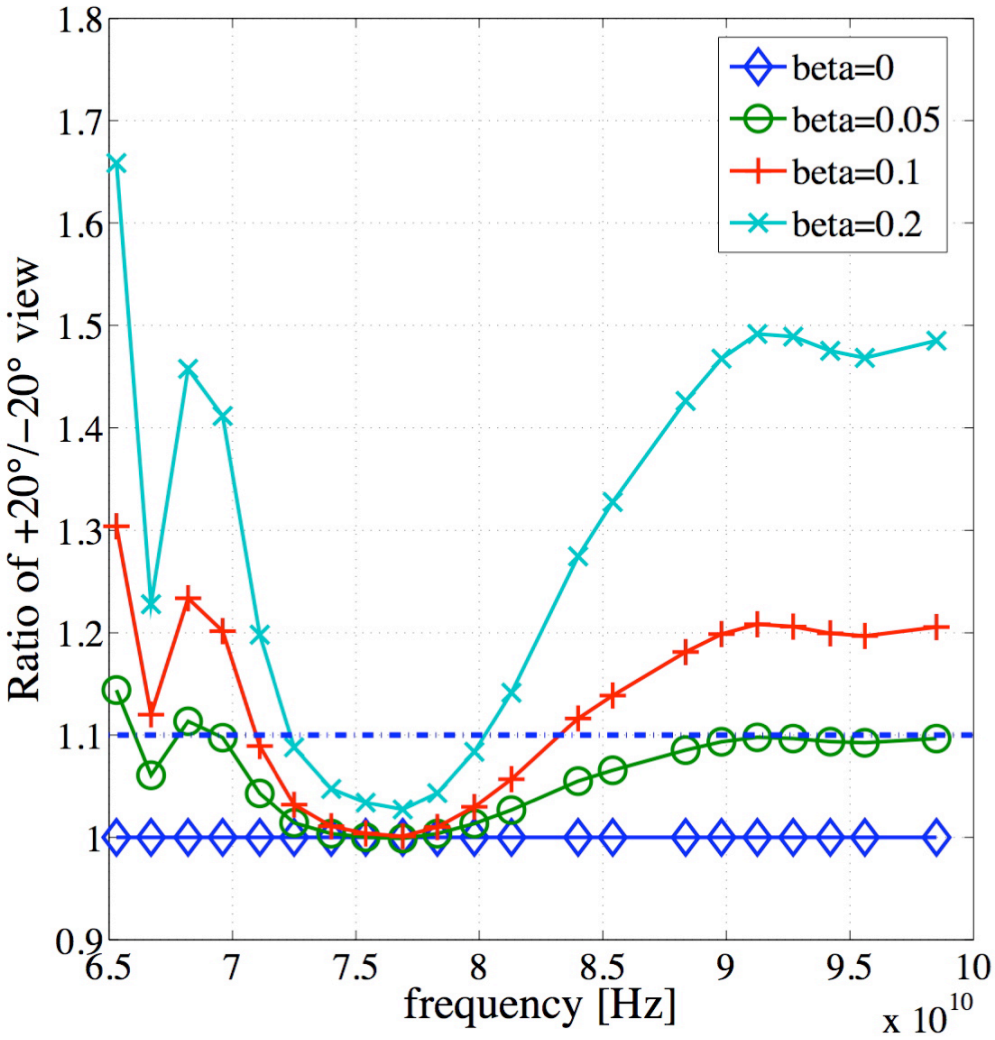

First measurements of oblique ECE with a real-time moveable line-of-sight on TCV, TP Goodman, Figure 11

REFERENCES

[1] P. BLANCHARD, *"Etudes du Rayonnement Suprathermique Emis lors du Chauffage Cyclotronique Electronique du Plasma du Tokamak TCV"*, Ph.D. Thesis, Ecole Polytechnique Fédérale de Lausanne, 2002.

[2] I. KLIMANOV, *"Reconstruction of the Electron Distribution Function During ECRH/ECCD and Magnetic Reconnection Events in a Tokamak Plasma"*, Ph.D. Thesis, Ecole Polytechnique Fédérale de Lausanne, 2006.

[3] S. ALBERTI, *et al.*, Nucl. Fusion **42,** 42-45 (2002).

[4] P. BLANCHARD, *et al.*, Plasma Phys. Control. Fusion **44,** 2231-2249 (2002).

[5] I. KLIMANOV, *et al.*, Rev. Sci. Instrum. **76**, 093504 (2005); I. Klimanov, *et al.*, *"Generation of suprathermal electrons during sawtooth crashes in a tokamak plasma"*, submitted to Plasma Phys. Control. Fusion.

[6] V.S. UDINTSEV, *et al.*, "*Progress in ECE development on TCV*", in Proc. of EC-14, Santorini, Greece (2006); V.S. UDINTSEV, *et al.*, *"Overview of Recent Results of ECE on TCV"*, Fusion Sci. Technol., to be published.

[7] A. MUECK *et al.*, *"Electron Bernstein Wave Heating in the TCV Tokamak"*, 47th Annual Meeting of the Division of Plasma Physics (Denver 2005), FP1.00062; A. MUECK *et al. "Electron Bernstein Wave Heating and Emission in the TCV Tokamak"*, Fusion Sci. Technol., to be published.

[8] M BORNATICI and U RUFFINA, Plasma Phys. Control. Fusion **38,** 1561–1577 (1996).

[9] E. DE LA LUNA, *et al.*, Rev. of Sci. Instrum. **74**, 1414-1420 (2003).

[10] T.P. GOODMAN, *et al.*, in Proc. 19th SOFT, Lisbon, 565 (1996).

[11] G. ZUANG, *et al.*, Plasma Phys. Control. Fusion **47,** 1539-1558 (2005).

[12] T.P. GOODMAN, *et al.*, *"Poloidally Asymmetric Plasma Response during ECH Experiments in TCV"* in Proc. of the 26th EPS Conf. on Plasma Phys., Maastricht, The Netherlands, P3.040 (1999); M.A. HENDERSON, *et al.*, Fusion Eng. Design **53**, 241-248 (2001).

[13] I. FURNO, *et al.,* Nucl. Fusion **41**, 403-420 (2001)

[14] R.M.J. SILLEN, Rijnhuizen Report 86-165 (1986).

[15] V.S. UDINTSEV et al., Rev. Sci. Instrum. **72**, 359 (2001).

[16] G. GIRUZZI *et al.,* Phys. Rev. Lett. **91**, 135001 (2003).

[17] Y. NAKAMURA, *et al., "Simulation Modeling of Fully Non-Inductive Buildup Scenario in High Bootstrap Current Tokamaks without Center Solenoids",* in Proc. of 32nd EPS Conference on Plasma Phys. Tarragona, 27 June - 1 July 2005 ECA Vol.29C, P-2.051 (2005)

[18] S. CODA, *et al.*, Nucl. Fusion **43,** 1361-1370 (2003).

[19] V. ERCKMANN and U. GASPARINO, Plasma Phys. Control. Fusion **36**, 1869-1962 (1994).